Journal of Materials Chemistry

Cite this: J. Mater. Chem., 2012, 22, 15275

www.rsc.org/materials

PAPER

Study of the antiferromagnetism of Mn_5Si_3: an inverse magnetocaloric effect material†

Michael Gottschilch,[a] Olivier Gourdon,*[bc] Joerg Persson,[d] Clarina de la Cruz,[e] Vaclav Petricek[f] and Thomas Brueckel[d]

Received 8th January 2012, Accepted 23rd May 2012
DOI: 10.1039/c2jm00154c

The intermetallic compound Mn_5Si_3 has been studied by high-resolution Time-of-Flight (TOF) neutron powder diffraction. At room temperature, Mn_5Si_3 is paramagnetic and it crystallizes in the $P6_3/mcm$ hexagonal space group. Magnetic susceptibility and specific heat measurements show clearly two major anomalies. At 100(1) K, a transition (Tm_1) corresponds to a collinear antiferromagnetic ordering (AF1). The second transition at 62(1) K (Tm_2), which was still unclear, highlights a magneto-structural distortion from an orthorhombic symmetry (AF1) to a monoclinic symmetry (AF2), which could be influenced by a low magnetic field. Such a magneto-structural change is directly associated with the inverse magnetocaloric effect behaviour of this material. A new description by means of the commensurate magnetic superspace groups, $Ccmm1'(0\beta0)00ss$ and $C2_1/m1'(\alpha\beta0)0ss$, has been used to refine properly the low temperature antiferromagnetic structures. Band structure calculations using the self-consistent, spin-polarized TB-LMTO method were accomplished to support the magnetic properties observed at low temperature.

Introduction

The MagnetoCaloric Effect (MCE), which is based on the entropy changes of magnetic materials in an applied magnetic field, holds the potential for numerous applications for cooling/heating processes without moving any mechanical parts. Consequently MCE has recently attracted the attention of many scientific groups.[1–8] The value of the MCE strongly depends on magnetic and structural changes influencing the entropy of the system. Indeed, the MCE is characterized by the isothermal magnetic entropy change ΔS and the adiabatic temperature change ΔT_{ad}, which are observed upon magnetic field changes. If the temperature derivative of the magnetization is negative, as is the case for the regular ferromagnetic materials, the thermodynamic formulation of the ΔS and ΔT_{ad} predicts $\Delta S < 0$ and $\Delta T_{ad} > 0$ (the direct MCE), *i.e.* the sample heats up when the external magnetic field is applied adiabatically. On the other hand, if the temperature derivative of the magnetization is positive, an opposite effect occurs, *i.e.* $\Delta S > 0$ and $\Delta T_{ad} < 0$ (the inverse MCE), the sample cools down when the external magnetic field is applied adiabatically. The inverse MCE, which is actually less common, exists in diverse kinds of magnetic arrangements; however it seems quite common in antiferromagnetic systems such as $MnBr_2 \cdot 4H_2O$ (ref. 9 and 10) and iron garnets $Y_3Fe_5O_{12}$, for example.[11] Preliminary research on the inverse MCE in antiferromagnetic compounds seems to associate the effect with a modification of magnetic sublattices under a magnetic field.[12,13]

As part of an effort to gain a better understanding of the inverse MCE, we reinvestigated the temperature and the field dependence of the magneto-structural distortions in Mn_5Si_3 which occur under 100 K. At low temperature, magnetic susceptibility and specific heat measurements show clearly two major anomalies at 100(1) K (Tm_1) and 62(1) K (Tm_2). A third anomaly, still under investigation, is also observed at 30(1) K and a magnetic hysteresis phenomenon occurs between 30 K and 60 K. All these features are associated with specific crystallographic and/or magnetic transitions which have been fully refined using TOF neutron powder diffraction data. The

[a]Jülich Center for Neutron Science JCNS-2 and Peter Grünberg Institut PGI-4, JARA-FIT, Forschungszentrum Jülich, 52425 Jülich, Germany. E-mail: m.gottschlich@fz-juelich.de
[b]Jülich Centre for Neutron Science outstation at Spallation Neutron Source, Oak Ridge National Laboratory, Oak Ridge, Tennessee 37831, USA. E-mail: gourdonoa@ornl.gov; Fax: +1 865 241 5991; Tel: +1 865 576 6629
[c]Chemical and Engineering Division, Spallation Neutron Source, Oak Ridge National Laboratory, Oak Ridge, Tennessee 37831, USA. E-mail: gourdonoa@ornl.gov; Fax: +1 865 241 5991; Tel: +1 865 576 6629
[d]Jülich Centre for Neutron Science JCNS and Peter Grünberg Institute PGI; JCNS-2, PGI-4: Scattering Methods Forschungszentrum Jülich GmbH52425, Jülich, Germany. E-mail: t.brueckel@fz-juelich.de
[e]Quantum Condensed Matter Division, Spallation Neutron Source, Oak Ridge National Laboratory, Oak Ridge, Tennessee 37831, USA. E-mail: delacruzcr@ornl.gov
[f]Institute of Physics ASCR v.v.i., Na Slovance 2, 182 21 Praha, Czech Republic. E-mail: petricek@fzu.cz

† Electronic supplementary information (ESI) available: Neutron crystallographic files in CIF format for the structure determination of Mn_5Si_3 at 90 K, 80 K, 70 K, 60 K, 50 K, 40 K, 30 K and 12 K. CCDC 862330–862337. For ESI and crystallographic data in CIF or other electronic format see DOI: 10.1039/c2jm00154c

magnetic structures have been solved using commensurate magnetic superspace groups, $Ccmm1'(0\beta0)00ss$ and $C2_1/m1'(\alpha\beta0)0ss$. In the light of the inverse magnetocaloric effect (MCE) observed at the Tm_2 transition, additional neutron powder diffraction experiments under a magnetic field have been performed and a magneto-structural distortion mechanism is proposed. Furthermore, band structure calculations using the self-consistent, spin-polarized TB-LMTO method were also accomplished to understand the electronic structure and to support the low temperature magnetic properties.

Experimental section

1. Synthesis

Mn_5Si_3 polycrystalline samples have been prepared by melting using the induced current method under argon. For further information on the preparation technique please refer to ref. 14 and references therein. Every batch was melted and annealed at least four times to get good quality samples. Mn (Aldrich, 99.99%) and Si (Aldrich, 99.99%) were used as starting materials. The Mn metal pieces have been preliminarily heated to remove the oxidation coating from the surface. All final products retain a metallic luster and are visibly stable upon exposure to both air and moisture over several weeks.

2. Magnetization measurements and heat capacity measurements

The dc magnetization as a function of temperature from 1.8 to 300 K was measured on a Quantum Design (QD) Magnetic Property Measurement System (MPMS). Temperature-dependent magnetization data were collected after the Mn_5Si_3 polycrystalline sample was placed in a gel capsule fixed in a straw by first measuring zero-field cooled (ZFC) magnetization and then the field-cooled (FC) magnetization. The specific heat measurements were performed on a Quantum Design PPMS-equipment.

3. TOF and CW neutron powder diffraction

Since at low temperature Mn_5Si_3 presents complex and various magnetic structures TOF neutron powder diffraction was performed. TOF neutron data were collected at the Spallation Neutron Source (SNS), Oak Ridge National Laboratory on the new powder diffractometer POWGEN. Differing from nearly all other time-of-flight (TOF) neutron powder diffractometers, the design of POWGEN is based on combining the diffracted neutrons collected at all angles into a single profile rather than assigning them to a series of different profiles that traditionally were based on grouping detectors according to the scattering angle. Such a unique approach yields a high count rate while preserving good resolution $\Delta d/d = 0.0015$ at $d = 1$ Å. Further information on the design of POWGEN could be obtained by referring to ref. 15 and references therein. Data were collected at 300 K, 100 K, 90 K, 80 K, 70 K, 60 K, 50 K, 40 K, 30 K and 12 K in that specific order. For each temperature two data collections using two different center wavelengths (CWLs) have been used. Based on the actual POWGEN detector configuration, CWLs of 1.066 Å and 3.198 Å were chosen. The first CWL which covers the d-spacing from 0.29 Å to 3.09 Å was used to have accurate information on the nuclear structure as well as the atomic displacement parameters (ADPs) whereas the second CWL which covers the d-spacing from 1.47 Å to 7.21 Å can give access to any additional magnetic information at higher d-spacing.

Since the magnetic field was not a sample environment available at the time of the experiments on POWGEN, neutron powder diffraction data were also collected on the same sample at low temperature under 0 T and 3 T magnetic field on the high-resolution neutron powder diffractometer HB2A at the High Flux Isotope Reactor at Oak Ridge National Laboratory, using 12′-31′-6′ collimation and a wavelength of 2.41 Å {Ge (113)}. More details about the HB2A instrument can be found in ref. 16.

The crystallographic structures were refined using JANA2006 software[17] using the Mn_5Si_3 structure, known from the literature,[18] as a starting model. The refinements were performed using simultaneously the two banks (each of them being associated with a different CWL dataset) to obtain unit cell parameters, atomic positions, and ADPs. Background coefficient, scale factors, isotropic strain terms in the profile function and absorption were also refined for a total of 30 parameters using the centrosymmetric space group $P6_3/mcm$ for the room temperature paramagnetic phase. At low temperature additional magnetic reflections consistent with a long-range magnetic ordering are observed and have required magnetic structure refinement treatments. Such magnetic refinements were also performed using JANA2006.[17] The magnetic scattering formalism has been recently implemented into the program which used a unique concept of superspace groups to treat magnetic groups.[19] Using this approach, magnetic structures of Mn_5Si_3 at 90 K and below have been fully refined using the $Ccmm1'(0\beta0)00ss$ orthorhombic {from 90 K down to 70 K} and $C2_1/m1'(\alpha\beta0)0ss$ monoclinic {from 60 K down to 12 K} superspace magnetic groups, respectively. A full description of the low temperature magnetic structure refinements will be given in the section entitled "Results and discussion".

4. Electronic structure calculations

Theoretical electronic structures of various model structures of Mn_5Si_3 were calculated self-consistently by using the tight-binding, linear muffin-tin-orbital (TB-LMTO) method[20–23] within the atomic sphere approximation (ASA) using the Stuttgart code.[24] Exchange and correlation were treated in a local spin density approximation (LSDA).[25] All relativistic effects except spin–orbit coupling were taken into account using a scalar relativistic approximation.[26] Within the ASA, space is filled by overlapping Wigner–Seitz (WS) atomic spheres. The radii of these WS spheres were obtained by requiring the overlapping potential to be the best possible approximation to the full potential according to an automatic procedure.[27] The WS radii for the atomic sites determined by this procedure are in the ranges 1.4–1.535 Å for Mn sites and 1.455–1.481 Å for Si sites. The basis set included 4s and 4p orbitals for Si and 4s, 4p, and 3d orbitals for Mn. The reciprocal space integrations to determine the self-consistent total energies and charge densities, densities of states (DOS) curves, and crystal orbital Hamilton population (COHP)[28] curves were performed using the tetrahedron method[29] using 64 k-points, with all-model structures in the irreducible wedges of the corresponding Brillouin zones.

Results and discussion

1. Magnetic behaviour of Mn_5Si_3

Temperature dependence of the dc magnetic susceptibility and the reciprocal magnetic susceptibility is shown in Fig. 1a. Temperature dependence of the magnetic susceptibility indicates multiple features. Above 300 K, the reciprocal magnetic susceptibility obeys the Curie–Weiss law with a Curie–Weiss temperature (θ) equal to 5(1) K and an average value of the effective magnetic moment equal to 3.6(1) μ_B. A deviation from the Curie–Weiss law is observed in the temperature region 100–300 K indicating a possible magnetic short range order just above the Neel temperature. At 62(1) K the reciprocal magnetic susceptibility exhibits a sharp jump and then a rapid increase with increasing temperature. Below that temperature down to 30(1) K, the magnetic susceptibility curve exhibits magnetic hysteresis behaviour. Finally, at 30 K a second weaker change of the magnetic susceptibility is also observed. These last features are still under investigation, but based on our neutron diffraction refinements, it could be associated with weak rearrangement of the spins in the magnetic frustrated configuration (triangular arrangement of the spins). In Fig. 1b the field-dependent specific heat in the 50 K to 120 K temperature range is illustrated. A magnetic field of 3 Tesla has been used to detect any possible magnetic field effect on the specific heat. Two anomalies at about 62 K and 100 K are clearly observed. These anomalies were already suspected to respond to an applied magnetic field based on the susceptibility measurements and are associated with the transitions from the paramagnetic stage to the first magnetic ordering at Tm_1 = 100 K, then at about 62 K to the second magnetic transition (Tm_2). Both transitions have a different response to an external magnetic field. Indeed, at the Tm_2 transition, the magnetic field enhances the specific heat by a factor of two at 3 Tesla. In contrast, the magnetic field has only an insignificant effect on the Tm_1 transition.

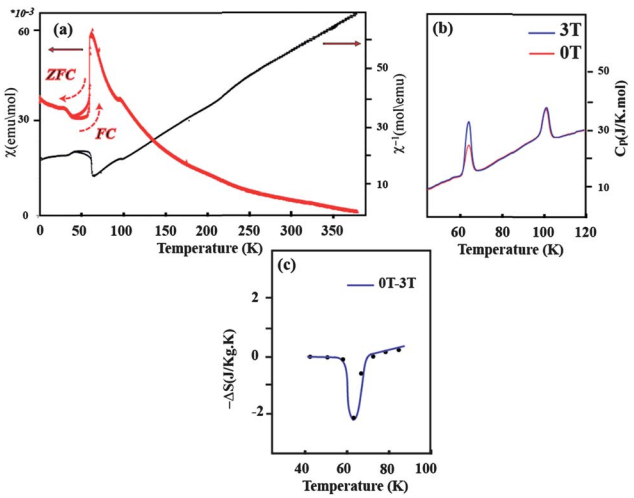

Fig. 1 Temperature dependence of the (a) dc magnetic susceptibility and the reciprocal magnetic susceptibility, (b) specific heat measurements under 0 T (red curve) and 3 T (blue curve) and (c) entropy change, between 0 T and 3 T, calculated based on the specific heat measurements using eqn (1)–(3). See text for details. Dashed arrows in (a) indicate the heating/cooling effect on the hysteresis loop.

Since the effect of the magnetic field at the Tm_2 transition suggested a MCE, entropy changes have been calculated (Fig. 1c) based on the field-dependent specific heat measurements. Indeed, MCE and magnetic entropy change can easily be determined from the temperature dependences of the heat capacity measured at various magnetic fields. This method has been previously used by Brown and Gschneidner and co-workers.[30] One of the advantages of this method is that it allows the determination of various parameters required for magnetic refrigeration design: heat capacity, total entropy, magnetic entropy change, MCE field and temperature dependences.

The total entropy of a material in a magnetic field $S(T,H)$ is defined using the following equation:

$$S(T,H) = \int_0^T \frac{C(T,H)}{T}\,dT + S_0 \quad (1)$$

where $C(T,H)$ is the field and temperature dependence of the heat capacity and S_0 is the entropy at 0 K, which is usually assumed to be equal to 0 based on the third law of the thermodynamics. Note that real measurements always start from a defined T_1 temperature which is different from 0. However, from the extrapolations Pecharsky and Gschneidner have proposed that the following equation can be used for the total entropy calculation based on experimental heat capacity data:[30]

$$S(T,H) = 0.5\left\{C(T_1,H) + \sum_{i=1}^{n}\left[\left(\frac{C(T_i,H)}{T_i} + \frac{C(T_{i+1},H)}{T_{i+1}}\right)(T_{i-1} - T_i)\right]\right\}^{45} \quad (2)$$

where n is the number of measured heat capacity data points between T_1 and T_n.

Therefore and by difference, from the calculated total entropy in zero magnetic field $S(0,T)$ and a final magnetic field $S(H,T)$, the magnetic isothermal entropy change at a defined magnetic field ΔS_{Mag} can be determined at any temperature T as follows:

$$\Delta S_{Mag}(H,T) = \Delta S(H,T) = S(H,T) - S(0,T) \quad (3)$$

Fig. 1c illustrates the entropy variation in the vicinity of the transition T_1. The maximum entropy $\Delta S_{Mag} \approx 2$ J kg^{-1} K^{-1} is observed at 62 K and most (half of the entropy change level) of the inverse MCE process arises between 60 and 70 K.

2. Nuclear/magnetic structure determination of Mn_5Si_3

To gain a better understanding of the structural/magnetic trend into that binary intermetallic phase, especially in the vicinity of the Tm_2 transition, where inverse MCE occurs, temperature-dependent neutron diffraction measurements on a polycrystalline sample of Mn_5Si_3 were conducted.

At room temperature, Mn_5Si_3 exhibits a hexagonal structure with space group $P6_3/mcm$ and lattice constants of $a = b =$ 6.91312(3) Å and c = 4.81735(3) Å. Its structure has been previously reported in the literature.[18] Fig. 2 shows the observed and calculated neutron diffraction patterns collected on POWGEN at 300 K. Refinement of the neutron data, which included

background coefficients, scale factors, profile functions, absorption coefficients, atomic position parameters and atomic displacement parameters, smoothly converged to a reasonable solution with a goodness of fit (gof) value of 1.18 ($R = 3.56\%$) for 36 parameters (9 atomic parameters + 27 profile parameters). Table 1 summarizes the refined atomic parameters and the equivalent ADPs. Note that the addition of anisotropic displacement parameters (ADPs) improves significantly the quality of the refinement. Two different sample batches have been tested for verification purposes and both of them show a slight elongation along the *c* direction of the Mn2 and Si atomic displacement ellipsoids. Table 2 summarizes the final atomic ADPs refined. The accuracy of the ADPs has been obtained by means of the high resolution data obtained at low *d*-spacing as presented in Fig. 2 (inset).

Fig. 3 illustrates a view of the Mn_5Si_3 hexagonal unit cell along the *c* axis. One classical way to explain this structure is to describe the local environments formed by the two Mn atoms (Mn1 and Mn2) which occupied the Wyckoff positions 4g and 6d, respectively. The Mn1 atom which is, at room temperature, surrounded by 6 equidistant Si atoms at 2.4305 (5) Å occupied a distorted octahedral site. This [Mn1Si$_6$] polyhedron is bicapped, through Si$_3$ triangular faces, by two additional Mn1 atoms. Thus, the Mn1–Mn1 distances are the shortest distances observed in the Mn_5Si_3 crystal structure with $d_{Mn1-Mn1} = 2.4089$ (5) Å. These [Mn1Si$_6$] polyhedra share triangular faces with their analogues to form quasi-infinite $^1{}_\infty$[Mn1Si$_3$] chains. Surrounding these chains Mn2 atoms are connected forming vacant [□(Mn2)$_6$] distorted octahedra with Mn2–Mn2 distances of 2.9054(3) Å. These [□(Mn2)$_6$] octahedra share triangular faces to form quasi-infinite $^1{}_\infty$[□(Mn2)$_3$] chains. This unique description based on the condensation of two quasi-infinite chains is illustrated in Fig. 4. This representation also has the advantage of investigating the stability of new closely related materials. Indeed, the □–Mn2 distance of 2.0256 (5) Å is suitable to accommodate small guest atoms such as boron, carbon or hydrogen. Therefore, by partially and/or totally filling the [□(Mn2)$_6$] octahedra, new materials could be synthesized.

In the vicinity of the Tm$_1$ transition, neutron powder diffraction data have been collected at 100 K, 90 K, 80 K and 70 K. Fig. 5 illustrates the observed and calculated diffraction patterns

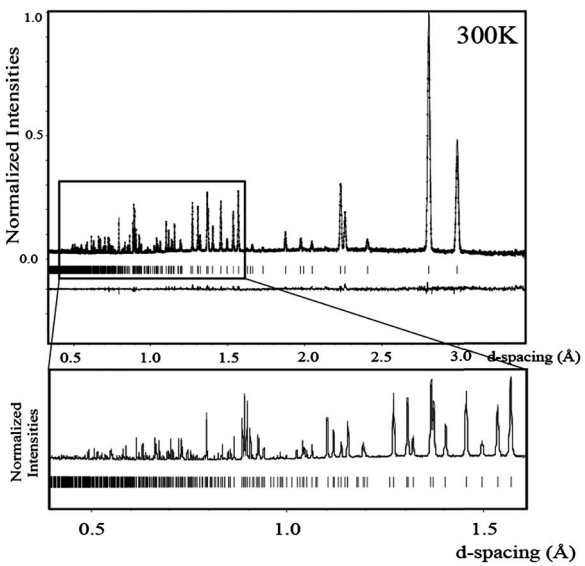

Fig. 2 Mn_5Si_3 neutron powder pattern obtained on POWGEN at 300 K. Dots indicate the normalized profile, the solid line is the calculated profile, tick marks below the profile indicate the positions of all allowed reflections, and the difference curve is shown below the tick marks on the same scale (*d*-spacing range 0.30–3.4 Å). The inset presents an expanded region of the *d*-spacing range between 0.40 and 1.60 Å.

Table 1 Atomic parameters and equivalent displacement parameters (Å^2) for Mn_5Si_3 at 300 K

Atom		*x*	*y*	*z*	U_{eq}
Mn1	4d	1/3	2/3	0	0.00517(16)
Mn2	6g	0.23583(10)	0.23583(10)	−1/4	0.0072(2)
Si	6g	0	0.40086(10)	−1/4	0.00648(17)

Table 2 Anisotropic displacement parameters (Å^2) for Mn_5Si_3 at 300 K[a]

Atom	U_{11}	U_{22}	U_{33}	U_{12}
Mn1	0.00498(19)	0.00498(19)	0.0055(3)	0.00249(10)
Mn2	0.0066(2)	0.0066(2)	0.0097(3)	0.0045(2)
Si	0.0045(2)	0.00491(19)	0.0099(3)	0.00224(12)

[a] $U_{13} = U_{23} = 0$.

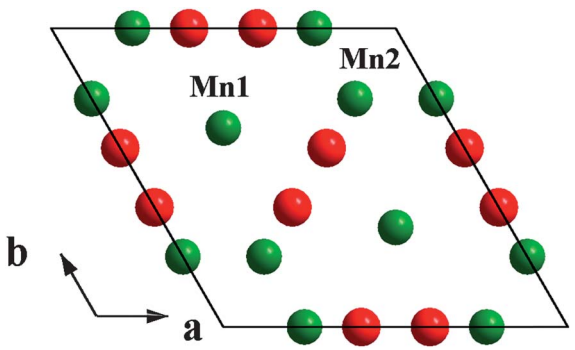

Fig. 3 View along the *c*-axis of the Mn_5Si_3 unit cell. Green and red spheres represent Mn and Si atoms, respectively.

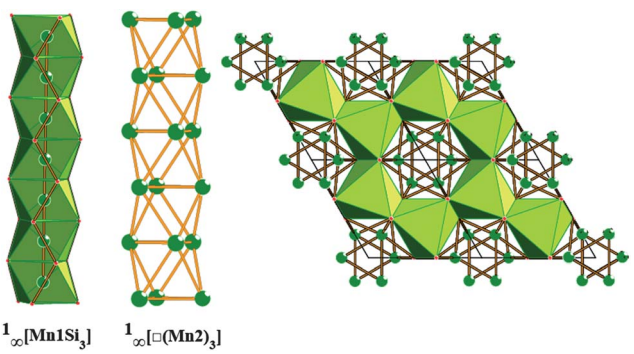

Fig. 4 Representation of the different connections between the polyhedra formed by the Mn1 and Mn2 atoms.

at 100 K and 90 K using short and large wavelength bandwidths as previously explained. The data collected at 100 K have been refined using the hexagonal structure with space group $P6_3/mcm$ already used to describe the room temperature data. The lattice constants converged to $a = b = 6.88965(2)$ Å and $c = 4.80011(2)$ Å with no significant atomic displacement. At 90 K the nuclear peak positions are not anymore consistent with the hexagonal symmetry and the orthorhombic space group $Ccmm$ ($P6_3/mcm$ subgroup) is necessary to explain the structural distortion. This orthorhombic unit cell is based on the ortho-hexagonal cell with $a = a_h$, $b = a_h + 2b_h$ and $c = c_h$, where a_h, b_h and c_h refer to the room temperature hexagonal unit cells. However, the refined orthorhombic cell parameters $a = 6.89695(2)$ Å, $b = 11.9085(3)$ Å and $c = 4.79666(3)$ Å, using the $Ccmm$ space group, show a significant distortion of the ortho-hexagonal unit. Indeed, the cell parameter a tends to increase whereas the cell parameter b decreases. Despite the structural distortion the unit cell volume between 100 K and 90 K stays almost constant.

The use of the orthorhombic subgroup $Ccmm$ implies the addition of a third independent Mn site. Indeed, the Mn2 atom in the hexagonal setting is equivalently described by the Mn21 atom and the Mn22 atoms in the orthorhombic subgroup (see Table 3). In addition to the peak splitting associated with the structural distortion, numerous extra peaks of the magnetic origin could be observed such as at ~3.3 and 3.4 Å and ~4.4 and 4.5 Å in d-spacing. These magnetic peaks are associated with a magnetic propagation vector along the orthorhombic b direction, as already observed by Brown *et al.*,[31] and could be indexed using the magnetic superspace group $Ccmm1'(0\beta0)00ss$ with $q = (0,\beta,0) = \beta^*$. After addition of magnetic wave(s) the refinement converges quickly with a satisfying gof value of 1.85 ($R = 3.28\%$) for 36 parameters. Table 3 summarizes the atomic parameters and the equivalent atomic displacements for Mn_5Si_3 at 90 K.

As already proposed by Brown *et al.*,[31] the 1D-magnetic (AF2) structure is quite simple with anti-parallel magnetic moments

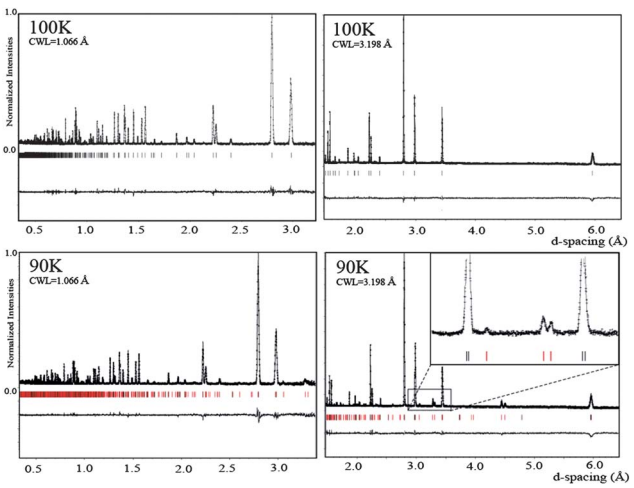

Fig. 5 Mn_5Si_3 neutron powder pattern obtained on POWGEN at 100 K and 90 K for the center wavelengths 1.066 Å and 3.198 Å. Dots indicate the normalized profile; the solid line is the calculated profile. Black and red tick marks indicate the positions of nuclear and magnetic reflections, respectively. The difference curve is shown below on the same scale. The inset presents characteristic magnetic peaks (see text for details).

Table 3 Atomic parameters and equivalent displacement parameters (Å^2) for Mn_5Si_3 at 90 K

Atom		x	y	z	U_{eq}
Mn1	8e	0	0.33245(14)	0	0.00208(15)
Mn21	4c	−0.2637(3)	0.5	−0.25	0.0011(3)
Mn22	8g	−0.6175(2)	0.38271(11)	−0.25	0.0035(2)
Si1	4c	0.1002(2)	0.5	−0.25	0.0023(4)
Si2	8g	−0.29949(19)	0.70028(10)	−0.25	0.0033(2)

carried exclusively on the Mn22 sites and pointing along the b direction (Fig. 6). The refined magnetic moment of 1.53(6) μ_B at 90 K is a value expected based on the literature[31] and from the susceptibility measurements. This result is valuable to validate the superspace approach to treat the magnetic structure and to extract accurate values.

Major reasons could explain why only one of the three Mn sites is carrying a moment at 90 K down to ~60 K. First of all, the Mn1–Mn1 distances are too short for any magnetic ordering to take place on this site. Secondly, the Mn21 atoms form triangular atomic arrangements with the Mn22 atoms implying a geometrically frustrated magnetic system.[32,33] Such magnetic frustration could also explain the nature of the short range ordering observed on the susceptibility measurements just above the magnetic ordering temperature. Further neutron powder diffraction data collected at 80 K and 70 K show similar orthorhombic magnetic ordering with refined magnetic moments on the Mn22 site of 1.74(6) μ_B and 1.89(6) μ_B, respectively. Simultaneously a tilt of the magnetic moments toward the Mn1 is observable (3° of tilt at 80 K and 8° of tilt at 70 K with respect to the b crystallographic direction).

At 60 K, high resolution neutron powder diffraction data highlight a change in the magnetic ordering. As illustrated in the inset of Fig. 7, the doublet of magnetic peaks (0 1 1 0) and (1 2 0 0) at ~4.5 Å in d-spacing turns into a triplet of magnetic reflections. Such a difference could only be explained by a monoclinic ordering of the spin. At first attempt the refinements at 60 K and below have used the magnetic superspace group $P2_1/m1'(½00)0ss$. However, to facilitate the comparison with the orthorhombic magnetic order, the use of the

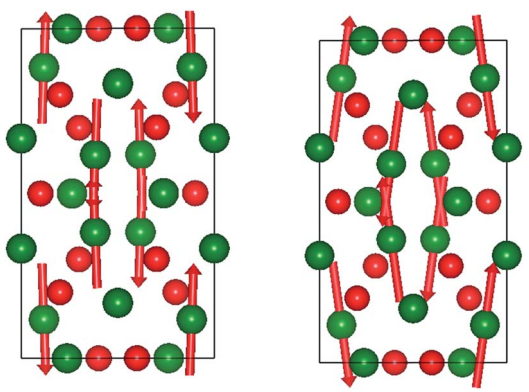

Fig. 6 View along the c direction of the refined magnetic structure of Mn_5Si_3 at 80 K (left) and 70 K (right). The arrows indicate the magnitude and the direction of the ordered moments (scale: 0.7 Å corresponds to 1 μ_B).

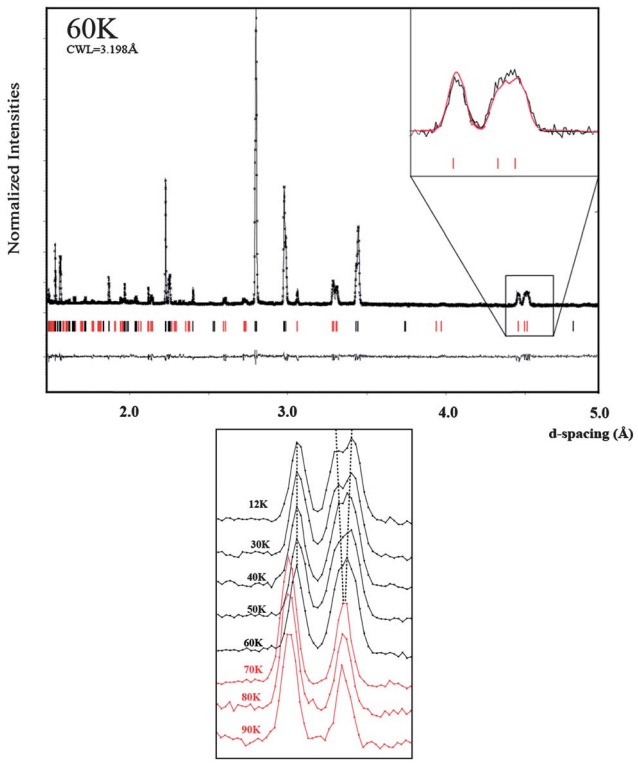

Fig. 7 (Top) Mn_5Si_3 neutron powder pattern obtained on POWGEN at 60 K for a center wavelength of 3.198 Å. Dots indicate the normalized profile; the solid line is the calculated profile. Black and red tick marks indicate the positions of nuclear and magnetic reflections, respectively. The difference curve is shown below on the same scale. The inset presents characteristic magnetic peaks (0 1 1 0) and (1 2 0 0) at around 4.5 Å (see text for details). (Bottom) The inset presents the trend of the magnetic peaks (0 1 1 0) and (1 2 0 0) in the *d*-spacing range 4.4–4.6 Å in the temperature range from 12 K to 90 K. Red and black curves indicate the existence of the orthorhombic or the monoclinic magnetic/nuclear symmetry.

non-standard setting $C21/m1'(010)0ss$ has been considered. This magnetic space group seems to be the most reasonable choice to explain simultaneously the nuclear and magnetic ordering. Various subgroups have been tested. However, none of them improve significantly the final magnetic model considered. Table 4 summarizes the cell parameters, atomic parameters and equivalent isotropic displacement parameters at 60 K, 50 K, 40 K, 30 K and 12 K. Fig. 8 illustrates the refined magnetic structure of Mn_5Si_3 at 60 K, 30 K and 12 K.

Despite the general good agreement of the observed and calculated diffraction patterns, the overestimation of the intensity of the (0 1 1 0) reflection is noticeable. To correct such imperfection in the refinement a weak magnetic moment on the Si2 site is necessary. Unfortunately, since no magnetic form factor is available for silicon an absolute moment value could not be refined. This polarization effect is a possibility since such a behaviour has already been observed in materials where metal and non-metal elements strongly interact.[34] Moreover, this result is consistent with our theoretical calculations presented thereafter. Such a discrepancy could also be explained by a small ferromagnetic canting of the spins.

Neutron diffraction of Mn_5Si_3 under a magnetic field. In order to investigate the magnetic field effect on the nuclear/magnetic structure, neutron diffraction under a magnetic field has been attempted on the neutron powder diffractometer HB2A at the High Flux Isotope Reactor at Oak Ridge National Laboratory. The results of this experiment collected at low temperature (50 K down to 5 K) under a magnetic field (4 Tesla) show evidence of a modification of the nuclear/magnetic structure of the material. The initial data collected at 50 K under no magnetic field are consistent with the results obtained from POWGEN data: cell parameters $a = 6.8968(3)$ Å, $b = 11.9052(5)$ Å, $c = 4.8081(4)$ Å and $\gamma = 90.218(3)^\circ$ with $V = 394.80(2)$ Å^3 using the monoclinic superspace group $C2_1/m1'(010)0ss$. Despite some lack of information at high-Q as well as a lowest resolution at high-*d* spacing, the addition of the magnetic field, as presented in Fig. 9, shows clearly a change in configuration/symmetry from the monoclinic to the orthorhombic symmetry. Indeed, data collected at 50 K under a 4 Tesla magnetic field have been refined using the superspace group $Ccmm1'(010)00ss$ with $a = 6.8853(3)$ Å, $b = 11.8589(5)$ Å and $c = 4.7914(4)$ Å with $V = 391.22(1)$ Å^3. This refinement indicates: (1) an annihilation of the magnetic moment on the Mn1 atomic site as observed above 60 K and (2) a contraction of ~1% of the cell volume. A test has been performed using the monoclinic symmetry but no noticeable improvement has been observed. Therefore and based on this observation, we could assume that the magnetic field is able to perturb the "soft" ferromagnetism associated with the Mn1–Mn1 coupling and so strengthen the stability of the orthorhombic AF2 arrangement.

Note that the orthorhombic symmetry observed at low temperature under 4 Tesla remains down to 5 K. Further experiments involving applied magnetic fields on POWGEN but also single crystal studies are underway to confirm this hypothesis.

Electronic structure calculations. Non-spin-polarized as well as spin-polarized calculations were performed to have a better understanding of the magnetic behaviour of this compound, especially the various magnetic couplings observed at low temperature. Different structural and magnetic models have been calculated based on the results obtained from the various neutron diffraction refinements. Optimisations of the crystal structures/atomic positions have been performed in agreement with the crystal symmetry confirming the results obtained by neutron diffraction refinements.

Nonmagnetic calculation on the Mn_5Si_3-hexagonal structure. In Fig. 10 the total densities of states (TDOS) and different partial densities of states (PDOS) for the non-spin-polarized calculations on the Mn_5Si_3 structure are presented. The PDOS of the Mn-3d orbitals and Si-4p orbitals are represented by green and red thick lines, respectively. The profile of the TDOS is close to the PDOS of the Mn-3d functions, which suggests that it dominates the electronic properties. The shape of the TDOS in the vicinity of the Fermi level corresponds mostly to two broad peaks: one centered around −2 eV and the second one centered on the Fermi level.

The Si-4p PDOS is relatively flat with the highest density around −3 eV, where small bonding interactions occur with the

Table 4 Unit cell parameters, atomic parameters, equivalent displacement parameters (Å^2) and magnetic atomic moments M (μ_B) for Mn_5Si_3 at 60 K, 50 K, 40 K, 30 K and 12 K using the superspace group $C21/m1'(010)0ss$

Atom		x	y	z	U_{eq}	M
60 K						
Cell parameters: $a = 6.8924(4)$ Å, $b = 11.9164(5)$ Å, $c = 4.80483(4)$ Å and $\gamma = 90.200(3)°$						
Mn1	4f	−0.0004(5)	0.3318(4)	−0.0056(7)	0.00141(15)	0.51(3)
Mn21	2e	0.2636(15)	0.5003(7)	0.25	0.0026(13)	2.21(4)
Mn22	2e	0.6172(16)	0.6170(5)	0.25	0.0018(3)	2.66(4)
Mn23	2e	0.6181(12)	−0.6185(8)	0.25	0.0017(12)	0.14(3)
Si1	2e	0.0989(17)	0.5002(8)	−0.25	0.0023(11)	0
Si2	2e	−0.2999(17)	0.3004(9)	−0.25	0.0030(12)	0
Si3	2e	−0.299(2)	−0.3000(7)	0.75	0.0024(3)	0
50 K						
Cell parameters: $a = 6.8929(3)$ Å, $b = 11.9152(5)$ Å, $c = 4.8061(4)$ Å and $\gamma = 90.222(3)°$						
Mn1	4f	−0.0008(4)	0.3314(3)	−0.0054(7)	0.00125(15)	0.53(3)
Mn21	2e	0.2639(13)	0.5000(7)	0.25	0.0026(11)	2.37(6)
Mn22	2e	0.6173(15)	0.6170(5)	0.25	0.0020(3)	2.80(6)
Mn23	2e	0.6184(12)	−0.6187(7)	0.25	0.0016(10)	0.15(3)
Si1	2e	0.0987(14)	0.5001(7)	−0.25	0.0025(10)	0
Si2	2e	−0.3001(14)	0.3006(7)	−0.25	0.0028(10)	0
Si3	2e	−0.2999(17)	−0.3000(6)	0.75	0.0024(3)	0
40 K						
Cell parameters: $a = 6.8931(2)$ Å, $b = 11.9150(4)$ Å, $c = 4.80675(3)$ Å and $\gamma = 90.247(2)°$						
Mn1	4f	0.0010(7)	0.3333(7)	−0.0046(9)	0.00141(14)	0.52(3)
Mn21	2e	0.2638(13)	0.5003(7)	0.25	0.0023(12)	2.40(6)
Mn22	2e	0.6170(14)	0.6169(5)	0.25	0.0010(2)	3.01(6)
Mn23	2e	0.6182(11)	−0.6189(7)	0.25	0.0010(11)	0.15(3)
Si1	2e	0.1003(14)	0.5008(7)	−0.25	0.0021(11)	0
Si2	2e	−0.3001(14)	0.2995(8)	−0.25	0.0028(12)	0
Si3	2e	−0.3006(16)	−0.2997(6)	0.75	0.0022(3)	0
30 K						
Cell parameters: $a = 6.8939(5)$ Å, $b = 11.9135(5)$ Å, $c = 4.80731(4)$ Å and $\gamma = 90.262(2)°$						
Mn1	4f	0.0000(6)	0.3322(6)	−0.0049(8)	0.00139(16)	0.51(3)
Mn21	2e	0.2633(14)	0.5002(7)	0.25	0.0026(13)	2.68(6)
Mn22	2e	0.6172(15)	0.6169(5)	0.25	0.0018(3)	2.95(6)
Mn23	2e	0.6182(12)	−0.6188(8)	0.25	0.0015(11)	0.17(3)
Si1	2e	0.0990(14)	0.5004(7)	−0.25	0.0016(10)	0
Si2	2e	−0.3001(14)	0.3004(8)	−0.25	0.0035(11)	0
Si3	2e	−0.3000(18)	−0.2999(6)	0.75	0.0025(3)	0
12 K						
Cell parameters: $a = 6.8943(3)$ Å, $b = 11.9131(5)$ Å, $c = 4.80742(5)$ Å and $\gamma = 90.268(3)°$						
Mn1	4f	0.0003(7)	0.3326(7)	−0.0055(7)	0.00142(15)	0.52(3)
Mn21	2e	0.2634(14)	0.5003(7)	0.25	0.0029(13)	2.60(6)
Mn22	2e	0.6175(15)	0.6169(5)	0.25	0.0018(3)	2.97(6)
Mn23	2e	0.6181(11)	−0.6188(8)	0.25	0.0014(12)	0.19(3)
Si1	2e	0.0992(15)	0.5005(7)	−0.25	0.0017(11)	0
Si2	2e	−0.3002(15)	0.3001(9)	−0.25	0.0034(12)	0
Si3	2e	−0.3003(18)	−0.2999(6)	0.75	0.0027(3)	0

Mn-3d orbitals. Integration of the Mn-3d shows that approximately 60% of the 3d states are occupied. As presented in Fig. 4, Mn occupies two different crystallographic sites which are based on octahedral and/or distorted octahedral sites. Therefore, the two broad peaks previously discussed reflect the (t_{2g}/e_g) orbital splitting which is actually more an (a_1/e′/e″) orbital degeneracy due to the distortion toward a trigonal prismatic local environment. The presence of two Mn sites implies also different types of Mn–Mn interactions. Indeed, based on the structural arrangement it is possible to identify short Mn1–Mn1 distances at 2.40 Å, Mn2–Mn2 distances at 2.81 Å and Mn1–Mn2 distances at 2.96 Å. These three different types of Mn–Mn interactions are illustrated by means of a COHP (crystal overlap Hamilton population[28]) analysis in Fig. 10. Using this analysis, it is possible to attribute the first peak around −3 eV to Mn–Mn bonding interactions, whereas the second one close to the Fermi level corresponds to Mn–Mn antibonding states. In Mn_5Si_3, the highest populated states correspond to Mn2–Mn2 nonbonding. Indeed, the Fermi level corresponds perfectly to the crossing between the bonding and the antibonding states among Mn2–Mn2 interactions. However, the Fermi level for Mn_5Si_3 corresponds to antibonding states, close to nonbonding, for the Mn1–Mn1 interactions as well as Mn1–Mn2 interactions. Dronskowski *et al.* have already shown that a driving force for antiferromagnetism or ferromagnetism lies in the local nonbonding or antibonding character of the states around the Fermi level.[35] Consequently, according to the Stoner criteria[36] and on the basis of our previous work on similar compounds,[37,38] magnetic properties are expected for Mn_5Si_3, and spin-polarized calculations should be performed to fully understand their electronic structures. Indeed, Stoner presented in 1938 a predictive model of itinerant electron ferromagnetism by assuming an average spin field interacting with a single spin. The Stoner criterion can be expressed as:

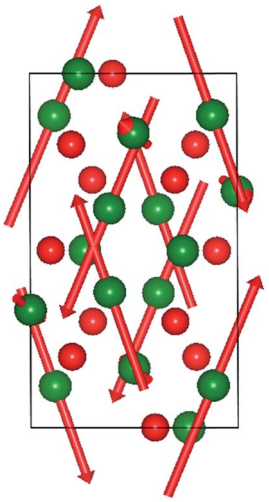

Fig. 8 View along the *c* direction of the refined magnetic structure of Mn_5Si_3 at 60 K. The arrows indicate the amplitude and the direction of the ordered moments (scale: 0.7 Å corresponds to 1 μ_B).

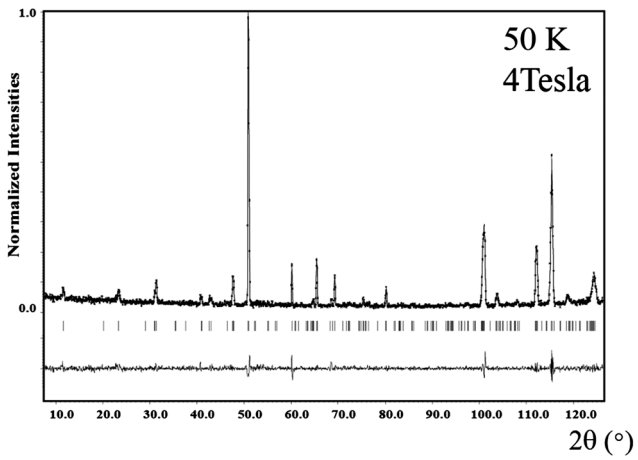

Fig. 9 Mn_5Si_3 neutron powder pattern obtained on HB2A at 50 K with a magnetic field of 4 Tesla. Dots indicate observed data and the solid line is the calculated profile. The difference curve is shown below on the same scale.

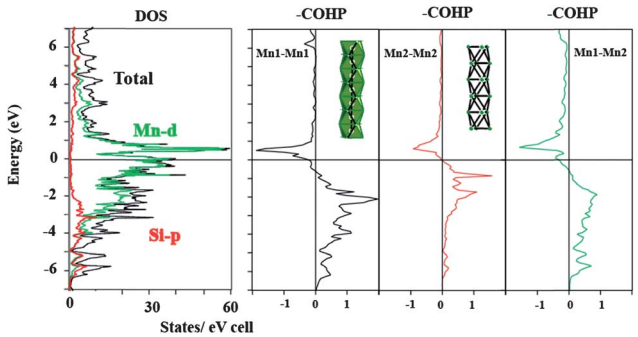

Fig. 10 Total DOS and Mn–Mn COHP curves for the Mn_5Si_3 hexagonal structure.

$$I \times \mathrm{DOS}(E_F) > 1$$

where I is a measure of the strength of the exchange interaction in the metal and DOS(E_F) is the density of states at the Fermi level, E_F. Nowadays, most solid-state physicists consider the Stoner criterion as a good indicator of whether a metal or an alloy will be ferromagnetic. The DOS(E_F) value is directly accessible by band structure calculations (the DOS(E_F) calculated is 31 states per eV per cell for Mn_5Si_3), and I values may be found in various papers. The first tabulation was created by Janak in 1977 (ref. 39) and gives I values for various single metals such as Cr (bcc), Mn (fcc), and Fe (bcc) as 0.38, 0.41, and 0.46 eV, respectively. Therefore, the Stoner criterion for Mn_5Si_3 is 1.27 per Mn atom. This value for the Stoner criterion is only a first approximation because I values for each atom are dependent upon the local environment. Nevertheless, spin ordering is expected and spin-polarized calculation should be performed to have a full understanding of the electronic/magnetic properties of Mn_5Si_3.

Spin-polarized calculations on Mn_5Si_3. Different initial magnetic models were attempted based on previously described hexagonal atomic arrangement. However, just one magnetic model was found to be more stable than the non-magnetic one with a favourable ΔE_{Tot} of 517 meV per unit cell. Finally, taking into account the structural distortion observed by neutron diffraction at 12 K (monoclinic distortion), a latest spin polarized model has been attempted. This latest model is by far the more stable as compared to the paramagnetic model (ΔE_{Tot} of 1.12 eV per unit cell). The final results for the spin-polarized calculations are listed in Table 5 and are qualitatively similar to the value refined by neutron diffraction (Table 4).

Fig. 11 illustrates the TDOS for the majority and minority spin electrons. The majority (spin-up) direction is indicated by ↑ and the minority (spin-down) direction by ↓. As presented in the nonmagnetic section the Mn states dominate the TDOS (not illustrated in the picture). Based on the various Mn–Mn distances and the nature of the crystallographic sites, three different Mn–Mn interactions could be described. These three different interactions could be associated with three different magnetic couplings: a $J1$ coupling between Mn1x–Mn1x atoms along the c direction, a $J2$ coupling between Mn2x–Mn2x atoms in the (ab) plane and a $J3$ coupling between Mn1x–Mn2x atoms. The spin polarized stable model confirms the speculation

Table 5 Results of spin-polarized band structure calculations obtained for Mn_5Si_3 with a monoclinic structural distortion[a]

Mn atoms	Magnetic moment (in μ_B)
Mn11	0.16(1)
Mn12	0.13(1)
Mn21	−1.82(1)
Mn22	2.23(1)
Mn23	−0.047(5)
Si1	0.010(4)
Si2	−0.020(4)
Si3	−0.003(3)

[a] Total magnetic moment of 1.29 μ_B per unit cell (/10 Mn).

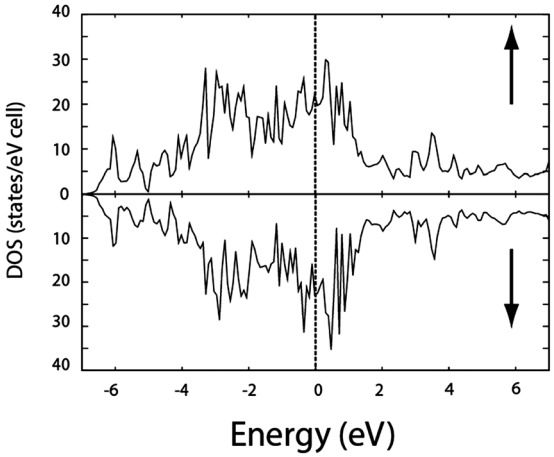

Fig. 11 Total density of states (TDOS) for the antiferromagnetic spin-polarized calculations on Mn_5Si_3.

already discussed based on the COHP study for the paramagnetic model. Based on our calculations, the *J*2 coupling is strongly antiferromagnetic whereas the *J*1 and *J*2 couplings are weakly ferromagnetic. This stable model represents fully the characteristic of the Mn_5Si_3 magnetic behaviour observed at low temperature.

The study of the partial density of states also confirms that a strong hybridization exists between the Mn(3d) and Si(3p) states. This strong hybridization is at the origin of a negative magnetic polarization on the Si atoms as suggested in Table 5. When compared to the nonmagnetic case (non-polarized), the Si(3p)–Mn(3d) hybridization is increased for the spin-up and decreased for the spin-down, due to an exchange splitting of the d block. As a consequence, the number of Si(p) states in the d block above the Fermi level is higher for the spin up than for the spin down and a negative magnetization appears. This statement and observation also confirm the importance of the nature of the non-metal element. Indeed, germanium which could substitute Si in that specific phase possesses more diffuse p orbitals and therefore an enhancement of the hybridization could be expected.

Conclusions

A new description using the $Ccmm1'(0\beta0)00ss$ and $C2_1/m1'(\alpha\beta0)0ss$ magnetic superspace groups has been presented to describe the magnetic ordering and therefore the magnetic couplings in the low temperature phases of Mn_5Si_3. Although Mn_5Si_3 possesses mostly an antiferromagnetic ordering, below 60 K some extra weak ferromagnetic couplings are observed and confirmed by theoretical calculations. Such a soft ferromagnetic behaviour seems to play a major role in the inverse MCE. Indeed, the magnetic field can easily act on its weak ferromagnetism and stabilizes the orthorhombic magnetic arrangement which will be unstable at that temperature without any magnetic field. Therefore, the energy associated with the entropy change is directly connected to the difference between the two magnetic configurations. Further neutron elastic and inelastic experiments are under way to fully elucidate the response to the magnetic field in this exotic class of materials.

Acknowledgements

The authors are grateful to Dr Ashfia Huq, Dr Jason Hodges, Luke Heroux and Mickael A. McGuire for their various constructive comments on the neutron experiments and the physical measurements. This research at Oak Ridge National Laboratory's High Flux Isotope Reactor and Spallation Neutron Source was sponsored by the Scientific User Facilities Division, Office of Basic Energy Sciences, U.S. Department of Energy. Development of the program Jana2006 was supported by Praemium Academiae of Czech Academy of Sciences.

References

1 E. Brück, O. Tegus, D. T. Cam Thanh, N. T. Trung and K. H. J. Buschow, *Int. J. Refrig.*, 2008, 763.
2 E. Brück, M. Ilyin and O. Tegus, *J. Magn. Magn. Mater.*, 2005, **290–291**, 8.
3 K. A. Gschneidner Jr, V. K. Pecharsky and O. A. Tsokol, *Rep. Prog. Phys.*, 2005, **68**, 1479.
4 S. Lin, O. Tegus, E. Brück, W. Dagula, T. J. Gortenmulder and K. H. J. Buschow, *IEEE Trans. Magn.*, 2006, **42**(13), 3776.
5 A. M. Tishin and Y. I. Spichkin, *The Magnetocaloric Effect and its Applications*, Institute of physics, 2003, Series in condensed matter.
6 K. A. Gschneidner and V. K. Pecharsky, *Int. J. Refrig.*, 2008, **31**, 945.
7 V. K. Pecharsky and K. A. Gschneidner Jr, *J. Magn. Magn. Mater.*, 1999, **200**, 44.
8 K. A. Gschneidner and V. K. Pecharsky, *Annu. Rev. Mater. Sci.*, 2000, **30**, 387.
9 J. H. Schelleng and S. A. Friedberg, *J. Appl. Phys.*, 1963, **34**, 1087.
10 J. H. Schelleng and S. A. Friedberg, *Phys. Rev.*, 1969, **185**, 728.
11 K. P. Belov, E. V. Talalaeva, L. A. Chernikova and V. I. Ivanoskii, *Pisma JETP*, 1969, **9**, 671.
12 N. J. Kurti, *J. Phys. Radium*, 1951, **12**, 281.
13 C. G. B. Garrett, *Proc. R. Soc. London, Ser. A*, 1951, **206**, 242.
14 R. J. Sovie and G. R. Seikel, *Radio-Frequency Induction Heating of Low-Pressure Plasmas*, National Aeronautics and Space Administration, Washington, D.C., October 1967, Springfield, Va.: Clearinghouse for Federal Scientific and Technical Information.
15 A. Huq, J. P. Hodges, O. Gourdon and L. Heroux, *Z. Kristallogr. Proc. 1*, 2011, 127.
16 V. O. Garlea, B. C. Chakoumakos, S. A. Moore, G. B. Taylor, T. Chae, R. G. Maples, R. Riedel, G. W. Lynn and D. Selby, Overview of the high-resolution powder diffractometer at the high flux isotope reactor, *Appl. Phys. A: Mater. Sci. Process.*, 2010, **99**, 531.
17 V. Petricek, M. Dusek and L. Palatinus, Jana2006*: The Crystallographic Computing System*, Institute of Physics, Praha, Czech Republic, 2006.
18 H. Binczyska, Z. Dimitrijevic, B. Gajic and A. Szytula, *Phys. Status Solidi A*, 1973, **19**, 13.
19 V. Petricek, J. Fuksa and M. Dusek, *Acta Crystallogr., Sect. A: Found. Crystallogr.*, 2010, **66**, 649.
20 O. K. Andersen and O. Jepsen, *Phys. Rev. Lett.*, 1984, **53**, 2571.
21 O. K. Andersen, *Phys. Rev. B: Solid State*, 1975, **12**, 3060.
22 O. K. Andersen, O. Jepsen and D. Glötzel, in *Highlights of Condensed-Matter Theory*, ed. F. Bassani, F. Fumi and M. P. Tosi, Lambrecht, W. R. L., North-Holland, New York, 1985.
23 O. K. Andersen, *Phys. Rev. B*, 1986, **34**, 2439.
24 *The Stuttgart Tight-Binding LMTO-ASA Program, Version 4.7*, Max-Planck-Institut für Festkrperförschung, Stuttgart, Germany, 1998.
25 U. Von Barth and L. Hedin, *J. Phys. C: Solid State Phys.*, 1972, **5**, 1629.
26 D. D. Koelling and B. N. Harmon, *J. Phys. C: Solid State Phys.*, 1977, **10**, 3107.
27 O. Jepsen and O. K. Anderson, *Z. Phys. B: Condens. Matter*, 1995, **97**, 35.
28 R. Dronskowski and P. Blöchl, *J. Phys. Chem.*, 1993, **97**, 8617.
29 P. E. Blöchl, O. Jepsen and O. K. Andersen, *Phys. Rev. B: Condens. Matter*, 1994, **49**, 16223.
30 G. V. Brown, *J. Appl. Phys.*, 1976, **47**, 3673.
31 P. J. Brown and J. B. Forsyth, *J. Phys.: Condens. Matter*, 1995, **7**, 7619.

32 G. Toulouse, *Commun. Phys.*, 1977, **2**, 115.
33 G. H. Wannier, *Phys. Rev.*, 1950, **79**, 357.
34 F. Boucher, J. Gareh, O. Gourdon, M. Evain and C. J. O'Connor, *J. Solid State Chem.*, 1997, **131**, 326.
35 G. A. Landrum and R. Dronskowski, *Angew. Chem., Int. Ed.*, 2000, 1560E.
36 C. Stoner, *Proc. R. Soc. London, Ser. A*, 1938, **165**, 372.
37 O. Gourdon and G. J. Miller, *J. Solid State Chem.*, 2003, **173**, 137.
38 O. Gourdon, S. Bud'ko, D. Williams and G. J. Miller, *Inorg. Chem.*, 2004, **43**, 3210.
39 J. F. Janak, *Phys. Rev. B: Solid State*, 1977, **16**(1), 255.

